# **Nanoscale**



## COMMUNICATION

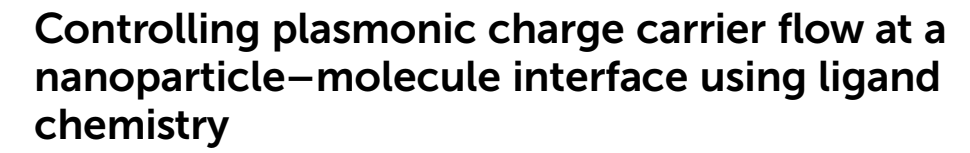
View Article Online



Cite this: DOI: 10.1039/d5nr02104a

Received 19th May 2025, Accepted 23rd September 2025 DOI: 10.1039/d5nr02104a

rsc.li/nanoscale



Gayatri Joshi, † Kalyani Patrikar, † Uditi Singhal, Anirban Mondal † and Saumyakanti Khatua †

Controlling charge-carrier flow at a metal-molecule interface is crucial for developing efficient plasmonic catalysts. Here, we demonstrate that the overlap of ligands' LUMO/HOMO with Au electronic states governs the flow of charge carriers induced by surface plasmon resonance (SPR) or interband excitation. A (p) NO2-Ph-SH functionalized gold nanoprism (NO2-TP) substrate exhibited a 4-fold higher hydrogen production rate compared to a (p)Br-Ph-SH-functionalized substrate (Br-TP) under interband excitation (440 nm). Conversely, under SPR excitation (740 nm) the Br-TP substrate exhibited a 10-fold higher hydrogen production rate than a NO2-TP substrate. Theoretical calculations reveal that the HOMO of (p)NO2-Ph-SH aligns effectively with the Au d-band, promoting d-band hole transport. In contrast, the LUMO of (p)Br-Ph-SH exhibits better overlap with the sp band above the Fermi level, enabling efficient hot electron transport. These findings provide general guidelines to optimize plasmonic catalysts for different excitation wavelengths.

#### Introduction

Photoexcitation of metal nanoparticles leads to high-energy electrons and holes forming before transferring their excess energy to the crystal lattice. These high-energy charge carriers could form *via* intraband (plasmonic excitation) and interband (atomic excitation) excitation, although their energies and locations in the metal could vary significantly. The intraband excitation generates low-energy (warm) holes near the Fermi level and high-energy hot electrons above the Fermi level. On the other hand, the interband excitation creates high-energy hot holes in the Au-d band and worm electrons near the Fermi Level. Carriers' lifetimes are different, with reports suggesting that the d-band holes created *via* interband excitation have longer relaxation times than the hot electrons produced by

Chemistry Discipline, Indian Institute of Technology Gandhinagar, Palaj, Gujarat-382055, India. E-mail: amondal@iitgn.ac.in, khatuask@iitgn.ac.in †These authors have contributed equally.

intraband transitions.<sup>1–5</sup> However, reports on opposite trends also exist.<sup>6,7</sup> Over the past decade, many reactions have been reported to be driven by hot electrons, holes, or simultaneous involvement of electrons and holes, albeit with low efficiencies due to the short lifetime of the charge carriers.<sup>8–14</sup>

Typically, hybrid nanostructures involving a plasmonic nanoparticle and co-catalyst are employed to improve the efficiency of the catalytic process. In such a hybrid "antennareactor" combination, the metal nanoparticle antenna absorbs photons and transfers the energy to the co-catalyst reactor via a direct energy transfer process<sup>15,16</sup> or can produce hot electrons and holes, which can subsequently move to the reactor.8,17-26 Preferential transfer of one of the charge carriers restricts the charge recombination processes, allowing the carriers to participate in chemical reactions. Over the past decade, several such nanohybrids consisting of plasmonic metal and semiconductor, non-noble metal, or molecular catalysts have been reported for hot electron-driven reactions where an empty band/LUMO of the reactor aligns with Au fermi energy (FE), allowing hot-electron transfer from the antenna to the reactor. 8,17,27-31 One would expect that this design principle could be generalized to d-band holes where a filled band/ HOMO of the reactor can be tuned for optimized overlap with the Au-d band, allowing better utilization of d-band holes which have recently been demonstrated to directly participate in the catalysis of a wide range of reactions. 4,6,32-36

Small organic molecules, such as substituted thiophenols, are ideal candidates for testing the validity of such a generalized approach. The easy substitution of the phenolic group offers an excellent method for tuning the HOMO/LUMO energies, which allows for control over their overlap with the gold Fermi level (FE) or d-band.<sup>37–41</sup> Furthermore, these molecules strongly bind to the gold surface *via* the Au–S bond, creating a stable system for photocatalytic studies. Previous reports suggest that they can enable pathways for the flow of energy or hot electrons from the metal to ligand, which may result in the damping of plasmons (chemical interface damping) or enhanced catalytic activities.<sup>31,42–50</sup>

Communication Nanoscale

In this study, we selected two substituted thiophenols, p-bromothiophenol (p-Br-Ph-SH) and p-nitro thiophenol (p-NO2-Ph-SH) ligands, and examined their effectiveness in controlling the transport of hot electrons and hot holes produced via intraband (at 740 nm) and interband (440 nm) excitation, respectively, by monitoring photocatalytic hydrogen production from water. Our choice of the ligand is based on detailed theoretical calculations (presented in a later section), which predict a better overlap between the ligand LUMO and Au FE for p-bromothiophenol functionalized nanoparticles (Br-TP) and the ligand HOMO and Au-d band for p-nitrothiophenol functionalized nanoparticles (NO2-TP). We observed that for interband excitation, NO2-TP significantly outperformed Br-TP, producing 4-fold more hydrogen. Conversely, for intraband excitation, Br-TP produced 10-fold more hydrogen than NO2-TP. Through theoretical analysis and further experiments, we attribute these observations to ligand-assisted charge carrier separation, enabled by selective transport of charge carriers: Au-d band hot holes in the case of NO<sub>2</sub>-TP and hot electrons in the case of Br-TP. These results provide a general strategy for developing efficient plasmonic catalysts for both interband and intraband excitation.

## Results and discussion

Br-TP and NO2-TP substrates were prepared by incubating AuTP-coated test tubes in 5 mM ethanolic solution of p-Br-Ph-SH or p-NO<sub>2</sub>-Ph-SH overnight (Fig. S2). The sample was then thoroughly washed with excess ethanol to remove any unbound chemicals. The ligand functionalization was consistent with a redshift in the LSPR peak, as shown in Fig. 1a. AuTP displayed an ~25 nm red shift upon binding with p-Br-Ph-SH and an ~60 nm red shift upon p-NO2-Ph-SH binding. The ligand binding was further confirmed through SERS analysis, as shown in Fig. S3. Due to the p-Br-Ph-SH attachment on the AuTP surface, the C-S and C-Br stretching at 1065 and 1078 cm<sup>-1</sup> was observed. Apart from this, the C-C stretching of the phenyl ring was observed at 1559 cm<sup>-1</sup>. On the other hand, for p-NO2-Ph-SH, apart from C-S and C-C stretching at 1078 and 1571 cm<sup>-1</sup>, the N-O stretch at 1335 cm<sup>-1</sup> confirms the attachment of the ligand onto the AuTP surface (Fig. S4).45 It is important to note that no S-H peak at 2560 cm<sup>-1</sup> or Si-H peak at 2100 cm<sup>-1</sup> was observed in SERS, confirming that no free thiol ligand or PMHS from the reaction solution was present on the substrates (Fig. S3). We performed ICP-OES analysis on both catalytic substrates to quantify the catalyst loading. The results indicated comparable amounts of gold and sulfur in each substrate, confirming that there was no significant difference in catalyst loading (Fig. S4). In addition, STEM-EDX mapping of both catalysts revealed a uniform thiol distribution across the entire AuTP structure (Fig. S5).

The photocatalytic hydrogen production from water was monitored for Br-TP,  $NO_2$ -TP, and bare-TP at neutral pH under 740 nm and 440 nm excitation (100 mW cm<sup>-2</sup> power density)

for 6 h. These wavelengths were selected to specifically excite the surface plasmon (740 nm) or the interband excitation (440 nm).

Plasmonic excitation is expected to produce high-energy electrons in the sp band above the Au FE and low energy holes in the sp band below the FE (a schematic description is shown in Fig. 1f). On the other hand, interband excitation is expected to produce highly energetic hot holes in the Au-d band and electrons in the sp band above the FE (Fig. 1e). Fig. 1b and c show the amount of photocatalytic hydrogen production from Br-TP (green), NO<sub>2</sub>-TP (red), and bare-TP (black) under 740 nm and 440 nm illumination, respectively. The bare-TP produced negligible hydrogen under 740 nm (Fig. 1b, black). The rate increased significantly, and a noticeable amount of hydrogen was produced (0.02 μmol mg<sup>-1</sup> h<sup>-1</sup>) under 440 nm excitation (Fig. 1d). Nonetheless, the bare-TP showed the least activity compared to the functionalized substrate at both wavelengths.

Both Br-TP and NO2-TP substrates produce significantly higher hydrogen than bare-TP, but their relative efficiency differs for interband vs. intraband excitation. The Br-TP substrate is found to be significantly more active under 740 nm (Fig. 1b, green), producing ~10 fold more hydrogen than NO<sub>2</sub>-TP (0.15 and 0.017 µmol mg<sup>-1</sup> h<sup>-1</sup> for Br-TP and NO<sub>2</sub>-TP respectively). Under 440 nm excitation, NO2-TP was found to be more active producing ~4 fold more hydrogen than Br-TP (0.29 and 0.067  $\mu$ mol mg<sup>-1</sup> h<sup>-1</sup> for NO<sub>2</sub>-TP and Br-TP, respectively). Interestingly, under 440 nm excitation, the hydrogen production rate of Br-TP decreased 2.5-fold (0.067 µmol mg<sup>-1</sup> h<sup>-1</sup>) than that under 740 nm excitation. On the other hand, the hydrogen production rate of NO2-TP increased 16-fold (0.29 μmol mg<sup>-1</sup> h<sup>-1</sup>) than that under 740 nm excitation. This reversal of activities is also consistent with calculated incident photon to hydrogen conversion efficiency (IPHCE) under 740 nm and 440 nm excitation (Fig. S6).

Several control experiments were performed to confirm that water is the source of hydrogen. There is a possibility that the H<sub>2</sub> may be produced due to the decomposition of the impurities that remain on the AuTP surface, such as unreacted free thiols or silane from the synthesis. The SERS analysis of the substrates before and after thiol functionalization confirms the absence of the Si-H peak at 2100 cm<sup>-1</sup> or the S-H from free thiol at 2560 cm<sup>-1</sup> (Fig. S3). To further confirm, we performed the photocatalytic experiment in the presence of acetonitrile instead of water under 740 nm illumination using Br-TP; no H<sub>2</sub> production was observed, confirming that the hydrogen originated from water. Another control experiment was performed where the photocatalytic experiment was conducted at >1000 nm excitation using a Br-TP substrate; at this wavelength, the incident photons will not have sufficient energy for water splitting but can perform photothermal Si-H activation in water and produce H<sub>2</sub> gas as reported elsewhere.<sup>51</sup> However, we did not notice any hydrogen production under these conditions. Furthermore, the simultaneous evolution of O2 with  $H_2$  was observed in GC with an  $H_2$ :  $O_2$  ratio of 1.9:1.0 for  $NO_2$ -TP at 440 nm and 1.8:1.0 for Br-TP at 740 nm, which is close to 2:1 expected from water splitting (Fig. S7a and b). These

d-band

Nanoscale

Bare-TF NO<sub>2</sub>-TP (a) **(b)** Interband (e) NO<sub>2</sub>-TP Br-TP (d-sp) Bare-TP 20 0.4 Extinction (a.u.) (hL/mg) sp-band  $\mathbf{FE}$ sp-band 5 d-band 900 1000 Wavelength (nm) Time (hr) ▲ NO<sub>2</sub>-TP 0.30 (c) 440 nm Intraband (f) (d) Br-TP (sp-sp) 40 Bare-TP 0.25 H<sub>2</sub> (µL/mg.hr) o H<sub>2</sub> (μmoles/mg.hr) 0.20 sp-band 0.15 sp-band 10 0.05

Fig. 1 (a) UV-visible extinction spectra of an AuTP functionalized glass test tube before (black) and after the surface modification with p-Br-Ph-SH (green) and p-NO<sub>2</sub>-Ph-SH (red) ligands. The inset shows the photograph of the AuTP functionalized test tube and its corresponding SEM image. (b and c) The photocatalytic HER was monitored under 740 nm (b) and 440 nm (c) illumination. The power for both light illumination was 100 mW cm<sup>-2</sup>. (d) The H<sub>2</sub> production rate was calculated for bare AuTP, Br-TP, and NO<sub>2</sub>-TP substrates under both light excitation. (e and f) Schematic representation of the hot carrier generation in metallic nanoparticles under interband and intraband transitions, respectively.

0.00

experimental observations confirm that hydrogen is produced from water.

Time (hr)

Now we discuss the plausible mechanism behind the differential activities of our substrates. None of the substrates produced hydrogen in the absence of LED excitation, indicating that the hydrogen production is driven by light excitation. The reaction could be driven by the plasmonic charge carriers or by the heat produced from their decay (photothermal effect).<sup>52</sup> To probe the photothermal aspect, we monitored the temperature rise of the reaction medium during the LED excitation. We notice temperature increases of 3.2 °C, 2.9 °C, and 4.0 °C under 440 nm and 3.8 °C, 3.3 °C, and 3.1 °C under 740 nm excitation for bare-TP, Br-TP, and NO2-TP substrates, respectively. We repeated the hydrogen production reaction with NO<sub>2</sub>-TP in the dark but at 40 °C, there was no production of hydrogen, indicating that the photothermal effect is not a major factor. Also, such a similar temperature rise cannot explain either the observed difference in substrate activities at a given excitation or the switching of their activities between 440 nm and 740 nm excitation. On the other hand, under 440 nm excitation, the hydrogen production rate of NO2-TP decreased drastically in the presence of a hole quencher (methanol). A similar trend was also observed for Br-TP under 440 nm excitation. The hole quencher also influenced the hydrogen production rate of the Br-TP substrate under 740 nm excitation, although the trend was opposite as the hydrogen production rate increased slightly (Fig. 2a).

NO2

Br

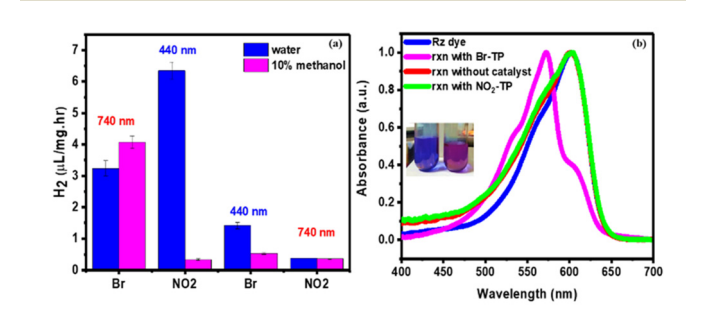


Fig. 2 (a) Photocatalytic H2 production rate observed for  $NO_2$ -TP and Br-TP in water and in the presence of a hole scavenger under 740 nm and 440 nm illumination. (b) Absorbance spectra of resazurin salt (RZ, blue), after photocatalytic reduction of Rz under 740 nm illumination using Br-TP (pink) and  $NO_2$ -TP (green), and without a catalyst (red).

Communication Nanoscale

To further ascertain the involvement of the hot carriers at 740 nm excitation, we studied the photoreduction of resazurin dyes by the Br-TP substrate, which led to a change of color from blue to purple, indicative of a hot carrier-driven reduction of resazurin to resorufin (Fig. 2b). These studies confirm that the observed hydrogen production is a hot carrier-driven process under both intraband and interband excitation. Thiol-based organic ligands have been reported to improve the photocatalytic efficiency of plasmonic nanoparticles in hot electron-driven processes. 38,45,53-55 In such cases, the ligands could facilitate the charge separation process either by quenching the holes by donating electrons from the HOMO or could allow transport of hot electrons to its LUMO. We conducted photocatalytic reactions with both Br-TP and NO2-TP in the presence of terephthalic acid. For the NO2-TP sample, a strong emission peak at 435 nm corresponding to 2-hydroxyterephthalic acid appeared after 5 h (Fig. S8b, red), indicating the generation of OH radicals during the catalytic process. In contrast, no OH radical formation was observed either under 740 nm illumination with NO2-TP or under 440 nm illumination with the Br-TP substrate (Fig. S8b, pink and green). However, a weak but noticeable fluorescence appears for Br-TP under 740 nm excitation (Fig. S8b, blue). Interestingly, the fluorescence intensities follow the same trend of the hydrogen production rate. These results confirm the hole-driven water oxidation process. The efficiencies of these processes are expected to depend on the overlap between metal and ligand orbitals and, therefore, we performed detailed theoretical calculations to understand the hole/electron transport in our substrates. No chemical changes of the ligand structures were noticed during the photochemical reaction (Fig. S9 and S10). While the nitro group is indeed a strong electron-withdrawing moiety and has potential for hydrogen bond formation with water, our results suggest that this interaction is not the dominant factor underlying the observed photocatalytic enhancement. Specifically, NO2-TP exhibited significantly higher activity only under 440 nm excitation (interband transition), while showing negligible activity under 740 nm excitation (intraband transition). If hydrogen bonding with interfacial water molecules were the primary mechanism, a comparable enhancement would be expected at both excitation wavelengths. Moreover, the Br-TP sample, which has a substantially lower propensity for hydrogen bonding with water, demonstrated 10-fold higher hydrogen production than NO<sub>2</sub>-TP under 740 nm illumination. This distinct wavelengthdependent behaviour strongly supports the conclusion that photocatalytic activity arises predominantly from hot-carrier contributions rather than hydrogen bonding interactions.

We now discuss the role of hot carriers in explaining the observed trends in photocatalytic water splitting across different substrates. Complete water splitting requires the participation of both hot electrons and holes. Since water oxidation is energetically demanding, it is widely recognized as the rate-limiting step, where the availability of sufficiently energetic holes becomes critical. Interband excitation at 440 nm is expected to generate a greater number of highenergy holes capable of driving water oxidation compared to that at 740 nm excitation. This expectation is consistent with our observation that the hydrogen production rate of NO2-TP under 440 nm illumination is significantly higher than those of both NO2-TP and Br-TP under 740 nm excitation. However, the presence of high-energy holes alone does not fully explain the activity trends, as Br-TP produced only a negligible amount of hydrogen under 440 nm excitation. We therefore propose that overall photocatalytic efficiency is governed not only by the energetic suitability of charge carriers but also by their effective separation, which is strongly influenced by ligandmetal interactions. Indeed, thiol-based organic ligands have been reported to enhance the photocatalytic performance of plasmonic nanoparticles in hot-carrier-driven processes. In such systems, ligands can facilitate charge separation either by quenching holes through electron donation from the HOMO or by supporting hot-electron transfer into the LUMO. The efficiency of these processes strongly depends on the orbital overlap between the metal and ligands, motivating us to perform detailed theoretical calculations to elucidate both hole and electron transport in our substrates.

The function of the ligand in the functionalized AuTPs is to facilitate the transfer of either holes or electrons from the Au nanoparticle to the reaction site. A ligand that increases the charge transfer can be considered effective. Fig. 3 shows the energy levels computed for the Au-ligand complex for Br-TP and NO2-TP from first principles. The energy levels of the molecular orbitals of the ligand are shown in red, and the states of the NP are displayed in blue. The highest occupied molecular orbital (HOMO) and lowest unoccupied molecular orbital (LUMO) are marked in the diagram in green. An electron is transferred from the AuNP to the LUMO of the ligand, while the hole is transferred to the HOMO of the ligand. The states of the AuNP participating in electron transfer are marked in cyan while those participating in hole transfer are marked in yellow. At an incident wavelength of 740 nm, an intraband transfer of electrons takes place, whereby the electron is excited from the sp band to energy levels greater than the Fermi level, marked in cyan in Fig. 3. The

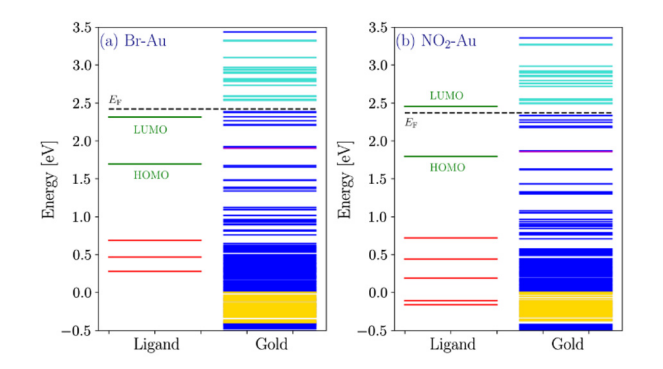


Fig. 3 Energy level diagrams for (a) Br-TP and (b) NO<sub>2</sub>-TP exhibiting states of the AuNP (blue) and ligand (red). The HOMO and LUMO of ligands are marked in green. States of Au participating in electron transfer are marked in cyan, while those participating in hole transfer are marked in yellow.

Nanoscale Communication

electron tends to transfer from these states to the LUMO of the ligand, which in both cases is at a lower energy level than the participating states of Au. The LUMO of Br-TP is at 2.36 eV, while the LUMO of NO<sub>2</sub>-TP is at 2.47 eV. Similarly, in the case of the incident wavelength being 440 nm, electrons tend to get excited from deeper energy levels in the d-band of the NP. This forms a hole in the d-band which transfers to the HOMO of the ligand. A higher rate of transfer in either case leads to higher catalytic activity.

We calculate the rate of charge transfer from the NP to ligand based on the Marcus-Hush equation:<sup>56</sup>

$$k = \int \frac{J^2}{\hbar} \sqrt{\frac{\pi}{\lambda kT}} n \, \exp\left(\frac{-(\lambda - \Delta E + q\eta)^2}{4\lambda kT}\right)$$

Here J refers to the charge transfer integral between the state of Au with n degenerate states, at an energy level having a difference of  $\Delta E$  with the relevant orbital of the ligand.  $\lambda$  refers to the reorganization energy of the ligand, and  $\eta$  refers to the overpotential of the surface, which could not be determined at this time, and has been considered as 0 for all calculations.<sup>57</sup>

J is obtained for the participating states and the HOMO or LUMO of ligands by calculations from first principles. Fig. 4 shows the values of J for Br-TP and NO<sub>2</sub>-TP, plotted against  $\Delta E$ , with histograms displaying the range of values among the various states. The values of J are plotted against the difference between participating state of Au and the LUMO in the case of electron transfer or the HOMO in the case of hole transfer. Fig. 4 (top panel) shows the values of I plotted against the

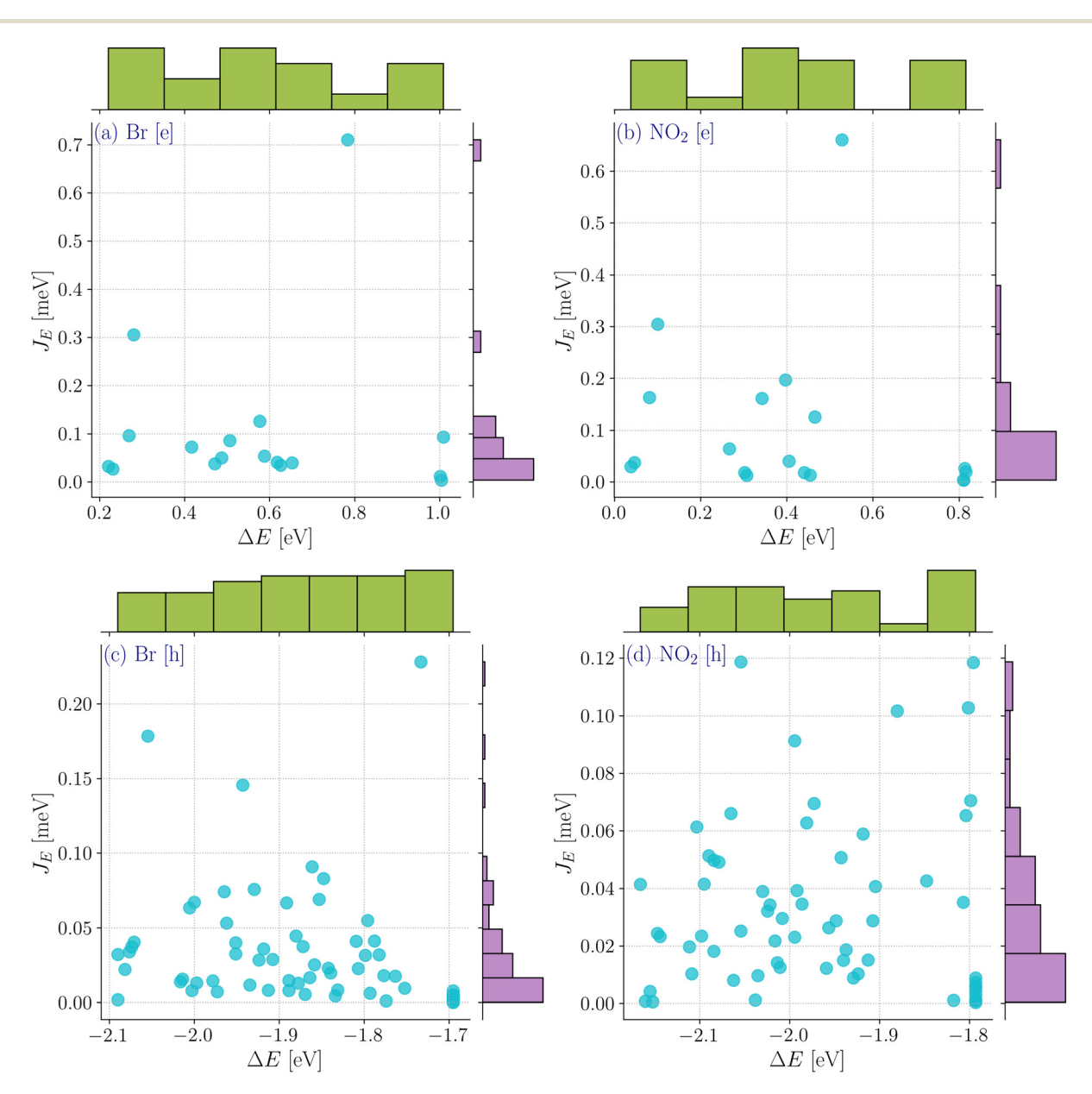


Fig. 4 Top panel: values of J between the LUMO and states participating in electron transfer plotted against ΔE for Br-TP and NO<sub>2</sub>-TP. Bottom panel: values of J between the HOMO and states participating in hole transfer for Br-TP and NO2-TP.

Communication Nanoscale

difference between each participating state of Au and the LUMO, for electron transfer. The ranges of J values are highly similar for photocatalysts with either ligand, between 0.0 eV and 0.3 eV for most of the states. However, the values of  $\Delta E$ are higher in the case of Br-TP, favoring a higher rate of electron transfer. Similarly, Fig. 4 (bottom panel) shows the values of J plotted against the difference between each participating state of Au and the HOMO, for hole transfer. Here too, the ranges of values of J are highly similar for photocatalysts with either ligand, 0.00 eV to 0.15 eV, with some states having a higher value for Br-TP. However, the participating states having a high value of I have a more negative  $\Delta E$  for NO<sub>2</sub>-TP, thereby favoring hole transfer. To analyze the cumulative effect of  $\Delta E$  and J over all states, the rate of charge transfer was calculated as per the Marcus-Hush equation. The rates of electron transfer calculated between relevant states of the AuNP and LUMO of the ligand are  $1.96 \times 10^9 \text{ s}^{-1}$  for Br-TP and  $1.03 \times 10^8$ s<sup>-1</sup> NO<sub>2</sub>-TP. The rates of hole transfer between the participating states and HOMO of the ligand are found to be  $8.72 \times 10^3$  $s^{-1}$  for Br-TP and 5.98 × 10<sup>6</sup>  $s^{-1}$  for NO<sub>2</sub>-TP.

Based on these theoretical calculations and experimental results, we now explain the catalytic activities of different substrates under interband and intraband excitation. For interband excitation at 440 nm, the hot holes are created in the d-band and lower-energy electrons near the Fermi level. Although these hot holes can in principle drive water oxidation, in the absence of suitable surface functionalization (e.g., hole- or electron-trapping ligands), they rapidly recombine before participating in any chemical process. As a result, in bare AuTP, most hot carriers undergo non-radiative relaxation, leading to minimal photocatalytic hydrogen evolution. The NO<sub>2</sub>-substituted ligand provides a better charge separation route compared to the Br-substituted ligand by allowing the d-band holes to transport from the metal to ligand. On the other hand, for intraband excitation at 740 nm, the Br-substituted ligand provides better charge carrier separation by allowing hot electron transport to ligands. The photocatalytic water splitting reaction involves both types of charge carriers and the efficiency of this process depends on the effective separation of these charges before their recombination, therefore making the NO2-TP substrate more active under interband excitation and the Br-TP substrate more active under intraband excitation.

### Conclusions

In conclusion, we demonstrate that the flow of plasmonic charge carriers generated via interband or intraband excitation at the metal-molecule interface could be controlled via ligand chemistry. A ligand with appropriate overlap of the HOMO and Au d-band could facilitate the separation of the charge carriers generated under interband excitation. On the other hand, a ligand with overlap between the LUMO and Au-sp band could facilitate the separation of the charge carriers generated under intraband excitation. These results provide an important

optimization strategy for the development of plasmonic catalysts for interband/intraband excitation.

### Author contributions

G. J. and S. K. conceptualized the work. G. J performed the synthesis, characterization of AuTP substrates, photocatalytic study, and data analysis. U. S. performs AuTP substrate preparation and surface modification. K. P. and A. M. performed theoretical DFT calculations. G. J., A. M., and S. K. wrote the manuscript. All authors have approved the final version of the manuscript.

#### Conflicts of interest

The authors declare no competing financial interest.

# Data availability

The data supporting this article have been included in the supplementary information (SI). Supplementary information: experimental details, supporting LSPR spectra, GC analysis, and SERS data. See DOI: https://doi.org/10.1039/d5nr02104a.

# Acknowledgements

We acknowledge the financial support from the Science and Engineering Research Board, India (CRG/2020/003471) and the Gujarat Council of Science and Technology (GUJCOST/2020-21/ 872), India. G. J. acknowledges support from the DST WISE-PDF fellowship (DST/WISE-PDF/CS-130/2023). We thank the central instrumentation facility (CIF) at IIT Gandhinagar for providing access to SEM and ICP-OES, Abira Rashid for assistance in STEM-EDX, Prof. Sameer Dalvi for the Raman Instrument, and Prashant Sharma for his assistance in SEM analysis. A. M. and K. P. acknowledge PARAM Ananta for computational resources.

#### References

- 1 C. Clavero, Nat. Photonics, 2014, 8, 95-103.
- 2 A. Lee, S. Wu, J. E. Yim, B. Zhao and M. T. Sheldon, ACS Nano, 2024, 18, 19077-19085.
- 3 S. Linic, S. Chavez and R. Elias, Nat. Mater., 2021, 20, 916-
- 4 P. Lyu, R. Espinoza and S. C. Nguyen, J. Phys. Chem. C, 2023, 127, 15685-15698.
- 5 Y. Kim, J. G. Smith and P. K. Jain, Nat. Chem., 2018, 10, 763-769.
- 6 G. Tagliabue, J. S. DuChene, M. Abdellah, A. Habib, D. J. Gosztola, Y. Hattori, W.-H. Cheng, K. Zheng,

S. E. Canton, R. Sundararaman, J. Sá and H. A. Atwater, *Nat. Mater.*, 2020, **19**, 1312–1318.

Nanoscale

- 7 J. Zhao, Y. Zhong, L. Zhang, L. Sui, G. Wu, J. Zhang, K. Han, Q. Zhang, K. Yuan and X. Yang, *Nano Lett.*, 2024, 24, 15340–15347.
- 8 S. Mubeen, J. Lee, N. Singh, S. Krämer, G. D. Stucky and M. Moskovits, *Nat. Nanotechnol.*, 2013, **8**, 247–251.
- 9 L. Zhou, M. Lou, J. L. Bao, C. Zhang, J. G. Liu, J. M. P. Martirez, S. Tian, L. Yuan, D. F. Swearer, H. Robatjazi, E. A. Carter, P. Nordlander and N. J. Halas, *Proc. Natl. Acad. Sci. U. S. A.*, 2021, 118, e2022109118.
- 10 M. Sun, A. Wang, M. Zhang, S. Zou and H. Wang, ACS Nanosci. Au, 2024, 4, 360–373.
- 11 F. Tong, X. Liang, X. Bao and Z. Zheng, ACS Catal., 2024, 14, 11425–11446.
- 12 E. Peiris, S. Sarina, E. R. Waclawik, G. A. Ayoko, P. Han, J. Jia and H.-Y. Zhu, *Angew. Chem., Int. Ed.*, 2019, **58**, 12032–12036.
- 13 J. S. DuChene, B. C. Sweeny, A. C. Johnston-Peck, D. Su, E. A. Stach and W. D. Wei, *Angew. Chem., Int. Ed.*, 2014, 53, 7887–7891.
- 14 Y. Liu, X. He, X. Liu, B. Li, J.-G. Ma and P. Cheng, *Angew. Chem., Int. Ed.*, 2025, **64**, e202422034.
- 15 K. Wu, J. Chen, J. R. McBride and T. Lian, *Science*, 2015, **349**, 632–635.
- 16 A. Jones, E. K. Searles, M. Mayer, M. Hoffmann, N. Gross, H. Oh, A. Fery, S. Link and C. F. Landes, *J. Phys. Chem. Lett.*, 2023, 14, 8235–8243.
- 17 H. Sheng, J. Wang, J. Huang, Z. Li, G. Ren, L. Zhang, L. Yu, M. Zhao, X. Li, G. Li, N. Wang, C. Shen and G. Lu, *Nat. Commun.*, 2023, 14, 1528.
- 18 H. Ren, J.-L. Yang, W.-M. Yang, H.-L. Zhong, J.-S. Lin, P. M. Radjenovic, L. Sun, H. Zhang, J. Xu, Z.-Q. Tian and J.-F. Li, *ACS Mater. Lett.*, 2021, 3, 69–76.
- 19 L. Yuan, J. Zhou, M. Zhang, X. Wen, J. M. P. Martirez, H. Robatjazi, L. Zhou, E. A. Carter, P. Nordlander and N. J. Halas, ACS Nano, 2022, 16, 17365–17375.
- 20 C. Yu, R. Zhan, S. Zhang, Z. Huang, J. Wang, G. Xie, L. Liao, H. Li, X. Xie, T. Ma and N. Zhang, *Nano Lett.*, 2024, 24, 9360–9367.
- 21 A. Schirato, S. K. Sanders, R. Proietti Zaccaria, P. Nordlander, G. Della Valle and A. Alabastri, ACS Nano, 2024, 18, 18933– 18947.
- 22 Y.-Q. Wang, J.-R. Zheng, Q. Liu, Y.-Q. Shi, H.-J. Liu, Z. Huang, J. Yi, Y. Yang and Q. Kuang, ACS Catal., 2024, 14, 6547–6557.
- 23 Y. Yang, H. Jia, N. Hu, M. Zhao, J. Li, W. Ni and C. Zhang, *J. Am. Chem. Soc.*, 2024, **146**, 7734–7742.
- 24 S. Liu, Z. Wu, Z. Zhu, K. Feng, Y. Zhou, X. Hu, X. Huang, B. Zhang, X. Dong, Y. Ma, K. Nie, J. Shen, Z. Wang, J. He, J. Wang, Y. Ji, B. Yan, Q. Zhang, A. Genest, X. Zhang, C. Li, B. Wu, X. An, G. Rupprechter and L. He, *Nat. Commun.*, 2025, 16, 2245.
- 25 B. Ostovar, S. A. Lee, A. Mehmood, K. Farrell, E. K. Searles, B. Bourgeois, W.-Y. Chiang, A. Misiura, N. Gross, A. Al-Zubeidi, J. A. Dionne, C. F. Landes, M. Zanni, B. G. Levine and S. Link, *Sci. Adv.*, 2024, **10**, eadp3353.

- 26 G. Sharma, R. Verma, S. Masuda, K. M. Badawy, N. Singh, T. Tsukuda and V. Polshettiwar, *Nat. Commun.*, 2024, 15, 713
- 27 Y. Fan, A. Girard, M. Waals, C. Salzemann and A. Courty, ACS Appl. Nano Mater., 2023, 6, 1193–1202.
- 28 Y.-C. Chen, Y.-K. Hsu, R. Popescu, D. Gerthsen, Y.-G. Lin and C. Feldmann, *Nat. Commun.*, 2018, 9, 232.
- 29 S. Lee, H. Hwang, W. Lee, D. Schebarchov, Y. Wy, J. Grand, B. Auguié, D. H. Wi, E. Cortés and S. W. Han, ACS Energy Lett., 2020, 5, 3881–3890.
- 30 M. Guan, J. Wang, K. Wang, J. Wang, R. Devasenathipathy, S. He, L. Yu, L. Zhang, H. Xie, Z. Li and G. Lu, J. Colloid Interface Sci., 2023, 633, 1033–1041.
- 31 Y. Chen, Y. Zhu, H. Sheng, J. Wang, C. Zhang, Y. Chen, W. Huang and G. Lu, *ACS Catal.*, 2022, **12**, 2938–2946.
- 32 J. Li, Q. Shen, J. Li, J. Liang, K. Wang and X.-H. Xia, *J. Phys. Chem. Lett.*, 2020, **11**, 8322–8328.
- 33 E. Kazuma, M. Lee, J. Jung, M. Trenary and Y. Kim, *Angew. Chem., Int. Ed.*, 2020, **59**, 7960–7966.
- 34 T. Peng, J. Miao, Z. Gao, L. Zhang, Y. Gao, C. Fan and D. Li, *Small*, 2018, **14**, 1703510.
- 35 A. E. Schlather, A. Manjavacas, A. Lauchner, V. S. Marangoni, C. J. DeSantis, P. Nordlander and N. J. Halas, J. Phys. Chem. Lett., 2017, 8, 2060–2067.
- 36 A. Al-Zubeidi, Y. Wang, J. Lin, C. Flatebo, C. F. Landes, H. Ren and S. Link, *J. Phys. Chem. Lett.*, 2023, 14, 5297– 5304.
- 37 M. Hollerer, D. Lüftner, P. Hurdax, T. Ules, S. Soubatch, F. S. Tautz, G. Koller, P. Puschnig, M. Sterrer and M. G. Ramsey, ACS Nano, 2017, 11, 6252–6260.
- 38 A. Stefancu, S. Lee, L. Zhu, M. Liu, R. C. Lucacel, E. Cortés and N. Leopold, *Nano Lett.*, 2021, 21, 6592–6599.
- 39 C. Boerigter, U. Aslam and S. Linic, *ACS Nano*, 2016, **10**, 6108–6115.
- 40 A. Stefancu, N. J. Halas, P. Nordlander and E. Cortes, *Nat. Phys.*, 2024, **20**, 1065–1077.
- 41 L. Shi and A. Troisi, ACS Catal., 2025, 6690-6701.
- 42 M. Guan, J. Wang, Z. Gong, K. Gao, X. Kang, Y. Zhang, C. Zhu, Z. Lu, X. Chen, L. Jiang, Q. Liu, H. Chen, L. Yu, K. Wang, Z. Li and G. Lu, *ACS Appl. Energy Mater.*, 2024, 7, 1329–1339.
- 43 M. Guan, Y. Zhu, X. Yue, Y. Liang, H. Sheng, J. Wang, C. Zhang, Q. Peng and G. Lu, ACS Appl. Nano Mater., 2021, 4, 10976–10984.
- 44 N. J. J. Johnson, B. Lam, R. S. Sherbo, D. K. Fork and C. P. Berlinguette, *Chem. Mater.*, 2019, 31, 8679–8684.
- 45 G. Joshi, R. Kashyap, K. Patrikar, A. Mondal and S. Khatua, *Nanoscale*, 2023, **15**, 16552–16560.
- 46 V. Jain, S. Roy, P. Roy and P. P. Pillai, *Chem. Mater.*, 2022, 34, 7579–7597.
- 47 V. Jain, R. K. Kashyap and P. P. Pillai, *Adv. Opt. Mater.*, 2022, **10**, 2200463.
- 48 B. Kafle, M. Poveda and T. G. Habteyes, *J. Phys. Chem. Lett.*, 2017, **8**, 890–894.
- 49 J. G. Smith and P. K. Jain, J. Am. Chem. Soc., 2016, 138, 6765-6773.

- Communication Nanoscale
- 50 Z. Zhang and J. Kneipp, J. Phys. Chem. Lett., 2021, 12, 1542-1547.
- 51 N. Kumar, A. Sharma, A. Bahirat, G. Joshi and S. Khatua, J. Phys. Chem. C, 2023, 127, 13484-13492.
- 52 R. Verma, G. Sharma and V. Polshettiwar, Nat. Commun., 2024, 15, 7974.
- 53 S. Roy, S. Roy, A. Rao, G. Devatha and P. P. Pillai, Chem. Mater., 2018, 30, 8415-8419.
- 54 S. Roy, V. Jain, R. K. Kashyap, A. Rao and P. P. Pillai, ACS Catal., 2020, 10, 5522-5528.
- 55 Z. Li, C. Zhang, H. Sheng, J. Wang, Y. Zhu, L. Yu, J. Wang, Q. Peng and G. Lu, ACS Appl. Mater. Interfaces, 2022, 14, 38302-38310.
- 56 N. S. Hush, J. Chem. Phys., 1958, 28, 962-972.
- 57 K. Patrikar, V. R. Rao, D. Kabra and A. Mondal, ACS Appl. Mater. Interfaces, 2023, 15, 49427-49435.